Two-dimensional Simulation of Richtmyer-Meshkov Instability

Amol Palekar *, Peter Vorobieff and C. Randall Truman

Department of Mechanical Engineering,
University of New Mexico,
Albuquerque, NM 87131, USA

Abstract

The Richtmyer-Meshkov Instability (RMI) arises when a density gradient in a fluid (gas) is subjected to an impulsive acceleration (e.g., due to a shock wave passage). The evolution of RMI is nonlinear and hydrodynamically complex and hence is a very good test problem to validate numerical codes. In this paper, a two-dimensional simulation of RMI is used to validate GASP, a structured, multi-block code that solves the Reynolds Averaged Navier-Stokes (RANS) equations. In this simulation, RMI is produced by shock acceleration of a diffuse heavy gaseous cylinder embedded in lighter gas. The predictions are compared with experimental measurements. Comparison of the late-time flow statistics between experiment and numerics elucidates the limitations inherently present in a two-dimensional simulation of a spatially three-dimensional flow, even if the large-scale flow structure is nominally two-dimensional.

Key words: Richtmyer-Meshkov instability, simulation, validation

1 Introduction

Richtmyer-Meshkov instability (RMI) occurs when an incident shock accelerates an interface between two fluids of different densities and thus amplifies any initial perturbation present on the interface. This interfacial instability was theoretically predicted in 1960 by a Los Alamos theorist, R.D. Richtmyer (Richtmyer, 1960), and first experimentally observed in 1969 by a Russian experimentalist, E.E. Meshkov (Meshkov, 1969). It is of importance to applications ranging from astrophysics (Arnett *et al.* , 1989), inertial confinement

* Email address: amolp@unm.edu (A. Palekar)

fusion (Lindl and Mead , 1975) to supersonic combustion (Fishbine , 2002; Marble *et al.*, 1987). The fluid configuration leading to a frequently considered RMI problem is shown in Fig. 1. Two fluids with different properties are separated by an initially diffuse interface. The shock travels from light fluid (gray color) to heavy fluid (black color) through the interface. The development of RMI for this configuration can be divided into three stages. The first stage is *linear - vortex driven*. In this stage, the incident shock wave collides with a perturbed material interface and bifurcates into a transmitted shock and a reflected wave. In Fig. 1, left, the pressure and density gradients are locally misaligned. This misalignment leads to baroclinic generation of vorticity at the interface. The resulting vortex roll-up (Fig. 1, right) leads to growth of the perturbation amplitude of the interface. The perturbation amplitude is very small as compared to the wavelength of the interface and hence the growth of interface can be safely assumed to be linear (Yang *et al.*, 1994; Richtmyer, 1960). Compressibility effects are important in this stage (Richtmyer, 1960). The flow-field in this stage is deterministic. Later in this stage, spikes and bubbles appear on the interface. A bubble is a portion of the light fluid penetrating into the heavy fluid and a spike is a portion of the heavy fluid penetrating into the light fluid.

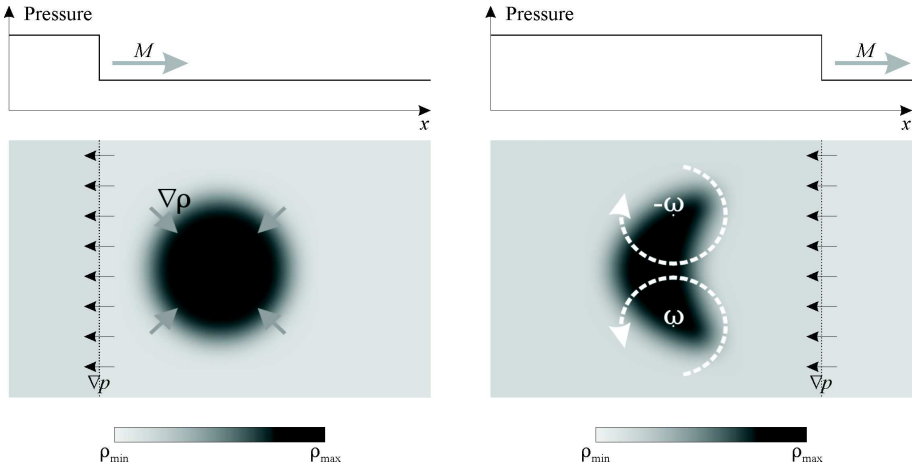

Fig. 1. Schematic representation of a planar shock acceleration of an initially diffuse cylindrical density interface: left – prior to acceleration, right – after acceleration. Note the initial misalignment between gradients of pressure (black arrows) and density (gray arrows) leading to deposition of vorticity (white dashed arrows). Note that this schematic does not represent many of the subtle effects in the flow, *e.g.*, shock reflection or focusing.

The second stage is *nonlinear deterministic*. In this stage the spikes and bubbles grow substantially. The amplitude of perturbation grows to the order of the wavelength and hence now the flow is nonlinear. In the later part of this stage, roll-up of material into the vortex cores occurs. Roughly at the same time, small scales also appear in the flow. The small scale appearing on the outer edge of the large scale vortex core may be due to shear-induced secondary instability while the small scale appearing on the inner edge may be

due to secondary baroclinic instability (Vorobieff *et al.*, 2004; Peng *et al.*, 2003; Zhang *et al.*, 2004). In this stage, the large scales in the flow are deterministic (Velikovich and Dimonte, 1996; Zhang and Sohn, 1996) while the small scales are stochastic. Rightley *et al* (1997) refer to this stage *ordered turbulence*. CFD codes can reliably predict the large scales but not the small scales (Rightley *et al*, 1999).

The third stage is *disordered turbulence* (Rightley *et al*, 1999). In this stage, the secondary instabilities become pronounced and lead to the onset of turbulence with chaotic mixing. Being turbulent in nature, this stage is dominated by three-dimensional physics, unlike the first two stages.

Figure 2 shows a schematic of the RMI evolution showing, from left to right, the initial conditions (Fig. 2 a) and following stages in the evolution: the linear stage (Fig. 2 b,c), the nonlinear growth of bubbles and spikes along with roll-up of material (Fig. 2 d), the small scales due to secondary instabilities (Fig. 2 e) and the chaotic turbulence (Fig. 2 f).

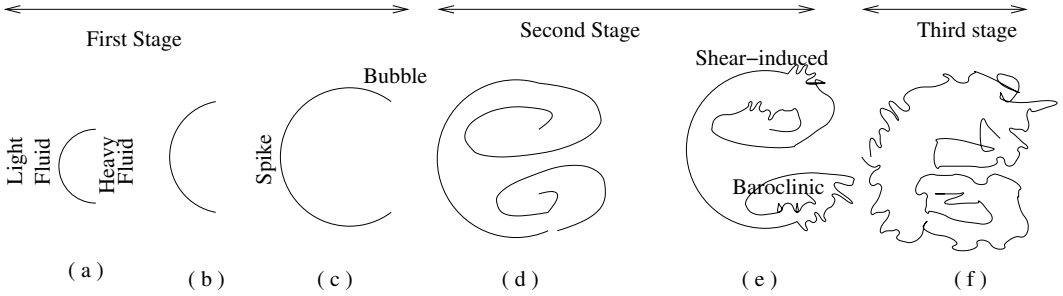

Fig. 2. Growth of Richtmyer-Meshkov Instability. Flow direction is from left to right.

The development of RMI depends heavily on the initial conditions that influence the vorticity deposition in the early stages of RMI evolution, and small changes in the initial conditions can lead to profound changes in the late-time flow morphology, as discussed by Budzinski and Benjamin (1994). RMI has several practical applications of importance (some of which were mentioned above), including strong explosions and inertial confinement fusion, which makes reliable numerical simulation of RMI-driven flows a priority. At the same time, the limited energy input into the RMI-driven flow, the gradual evolution of the initially deterministic flow towards disorder and the dependence on the initial conditions makes RMI an attractive problem for a more general study of transition to turbulence. Advances in experimental diagnostics in the recent years have produced highly resolved quantitative benchmarks that can be used to validate numerical codes. In this paper, we describe code validation results for a computational fluid dynamics (CFD) code extensively used for simulations of high-speed compressible mixing and reacting flows.

2 Problem Description

The objective of this paper is to validate GASP, a CFD code, using two-dimensional RMI as the test problem. As explained above, for RMI, the fluid configuration must have an initially perturbed (non-planar) density interface subjected to impulsive acceleration. A geometrically simple configuration for a validation program is shown in Fig. 1. A sulfur hexafluoride (SF_6) cylinder is immersed in air. The interface between the air and the heavier SF_6 is diffusive. The flow is impulsively accelerated by a planar Mach 1.2 shock. This problem has been the subject of several experimental studies described immediately below, producing flow visualization and qualitative data. The experimental results are compared with the results produced by a numerical simulation conducted with GASP.

2.1 Experimental Setup

The experiments were performed using the DX-3 shock tube at Los Alamos National Laboratory. The shock tube is 5.4 m long with a square cross-section of 7.5 cm. Figure 3 shows four main components of the shock tube: driver section, driven section, test section and end section. The driver section initially contains nitrogen pressurized to 140 kPa. The driver section and the driven section are separated by a diaphragm, which on rupture produces a planar Mach 1.2 shock. The interface between light gas (air) and heavy gas (SF_6) is created using a cylindrical contoured nozzle of diameter 0.8 cm. SF_6 enters from the top of test section and is exhausted through the bottom. This results in a nearly two-dimensional vertical SF_6 cylinder with a diffuse interface traversing the middle of the test section. Several visualization techniques (Mie scattering off glycol vapor droplets pre-mixed with SF_6, planar laser-induced fluorescence (PLIF)) can be employed for the study of the evolving flow. The flow evolution is observed in a planar section of the shock tube illuminated with a thin (0.1 - 1 mm) horizontal light sheet produced by a pulsed laser.

2.2 GASP

GASP is a CFD code from AeroSoft, Inc., Blacksburg, VA. We have used the export version GASPex 4.1.2 as the flow solver. GASP is a structured, multi-block CFD solver that solves the Reynolds Averaged Navier-Stokes(RANS) equations. GASP uses a fully conservative, cell centered, upwind, finite difference numerical scheme. It also has a dual time stepping algorithm, which along with the implicit time integration scheme provides greater stability at larger time steps. It is capable of predicting compressible flow of Mach 0.1 and

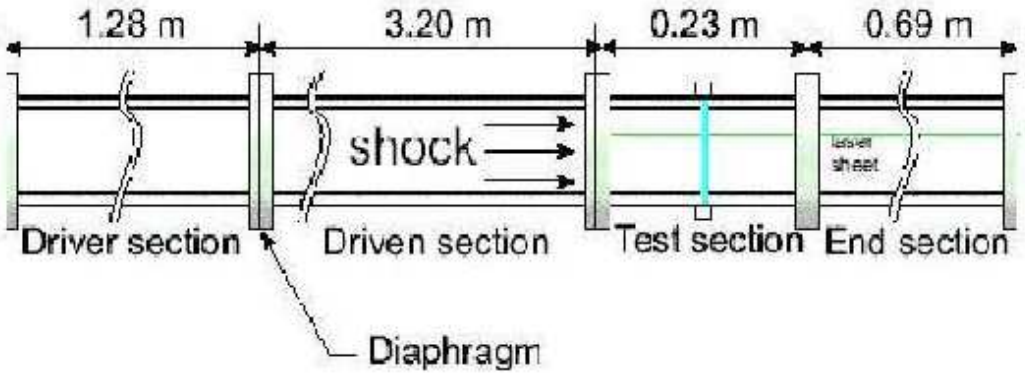

Fig. 3. Schematic of the shock tube. After Fig. 4 in Zoldi (2002)

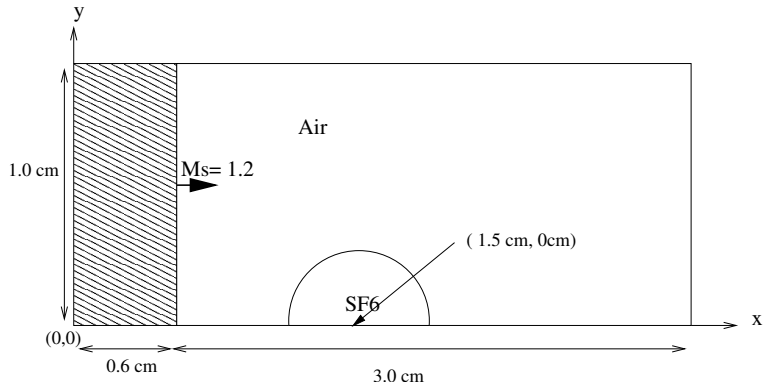

Fig. 4. Computational Domain.

greater. A wide variety of flows has been studied using GASP including flows in a combustion chamber and flows over reentry vehicles. GASP is being used by NASA for verification purposes (Aerosoft , 2004).

3 Numerical Simulation

The computational domain is shown in Fig. 4. We have tried to minimize the computational domain so as to decrease the computational time. The domain along the y-direction was reduced to 1.0 cm from the physical 3.75 cm half-width of the shock tube by applying reflective boundary condition at y = 1.0cm. The domain along the x-direction was reduced significantly as opposed to the physical length of the shock tube. This is achieved by using the upstream condition of the shock in the test section. The variation of pressure in the shock tube is shown in Fig. 5.

The pressure behind the shock drops from P_0 to P_1 and hence when the shock hits the SF_6 cylinder in the test section, it has upstream conditions corresponding to pressure P_1. These upstream conditions are specified as the

initial conditions for the shocked region (the shaded region in Fig. 4) and an inflow boundary condition is used at x = 0 cm. When the shock hits the SF_6 cylinder, it bifurcates into a reflected shock wave and a transmitted shock wave. The reflected shock does not affect the development of RMI. To achieve this numerically, we change the boundary condition at $x = 0$ to reflective, at the time when the front of the reflected shock wave reaches $x = 0$ cm. The evolving SF_6 cylinder has finite velocity and to ensure that it stays within the computational domain, a uniform negative velocity is superimposed on the flow in the x-direction. It is important to note that the SF_6 cylinder must not travel towards the $x = 0$ boundary because that would lead to interaction between the reflected shock and SF_6 cylinder.

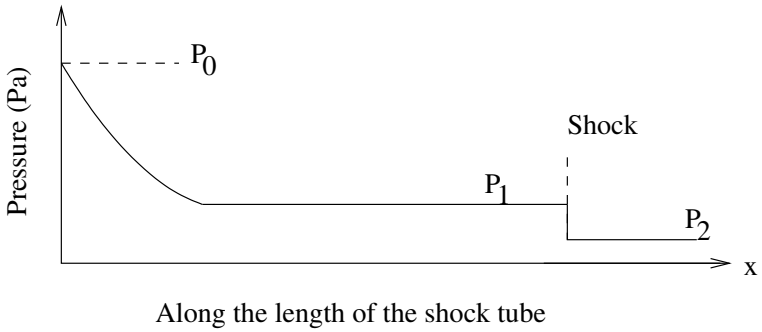

Fig. 5. Pressure variation along the shock tube.

The values for time step (Δt) and grid spacing (Δx) were found in a convergence study. In RMI, the moving shock has the highest propagating speed and this specifies the limiting values for Δt and Δx. Hence a one-dimensional moving shock problem was simulated to determine Δt and Δx . Grid sizes of 100 μm, 200 μm and 800 μm were used. Figure 6 shows the pressure time history as the shock passes a selected point in the flow. After obtaining convergence at $\Delta x = 200$ mm, different time steps (Δt) were used. As seen in Fig. 7, the solution converged for $\Delta t = 0.125$ μs. After the shock passed through the computational domain, the value for Δt was increased by a factor of 6.

Table 1
Initial Conditions

Property	Upstream of shock	Downstream of shock
Pressure (Pa)	121100	80000
x-velocity (m/s)	104.9	0
y-velocity (m/s)	0	0

Second-order accuracy in time and third-order accuracy in space were used to

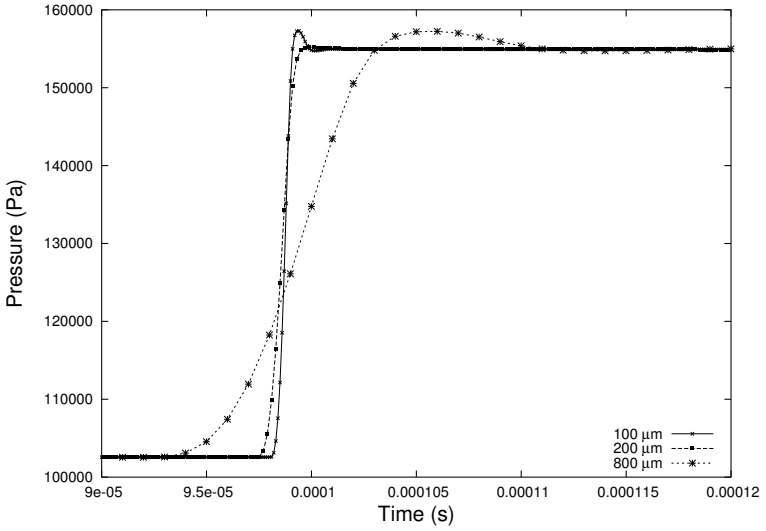

Fig. 6. Pressure time history for the 1-D model showing the effect of grid-spacing refinement with $\Delta t = 0.125$ μs.

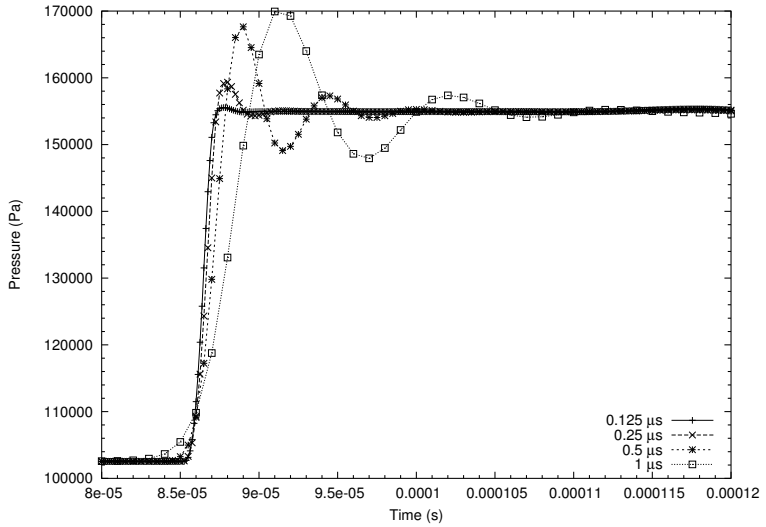

Fig. 7. Pressure time history for 1-D model showing the effect of time step reduction with $\Delta x = 200$ μm.

predict RMI-driven flow evolution. Roe's scheme was used for inviscid flux. For the viscous case, the Sutherland viscosity model was used. An implicit dual time stepping Gauss-Seidel scheme was used as the temporal algorithm. The initial conditions are shown in Table 1. The initial distribution of SF_6 is shown in Fig. 8 (Greenough *et al.*, 2001).

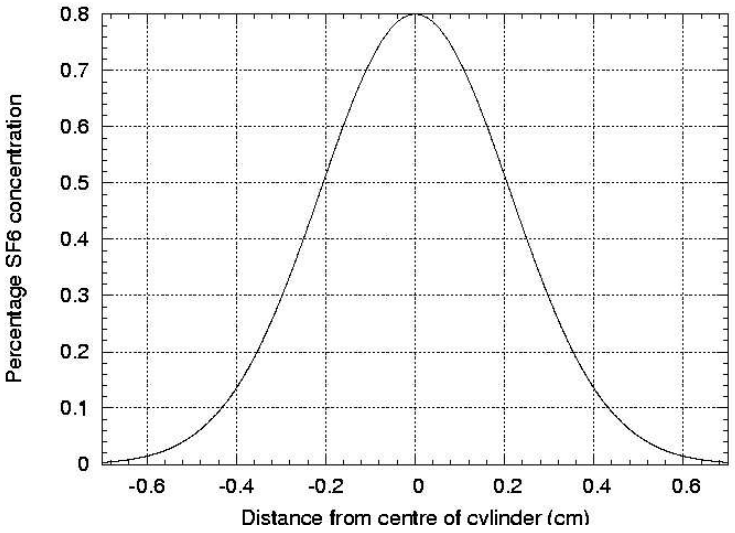

Fig. 8. Concentration distribution in initial conditions (Greenough *et al.*, 2001).

4 Results

The results from simulations are quantitatively and qualitatively compared with the experiments. The experimental single-cylinder data from the LANL DX-3 shock tube described earlier were published in several papers by Tomkins *et al.* (2002), Tomkins *et al.* (2003), and Vorobieff *et al.* (2003). Here we mostly use the work of Tomkins *et al.* (2003) for validation. Numerical simulation may not predict the physics accurately due to its discrete nature. Also the 2-dimensional assumption may not be valid at late times when secondary instabilities become important. Hence we have also done a comparison with the 2-dimensional simulations done by Greenough *et al.* (2001).

4.1 Mesh Size

The widths and heights of the mixing zone produced by shock acceleration of the SF_6 cylinder (illustrated in fig. 9a) and the spacing between the vortex cores of large scale counterrotating vortices (illustrated in fig. 9b) are used for quantitative comparison between experiment and simulation. Figures 10, 11 and 12 show the results for mesh spacing of 200 μm, 100 μm and 50 μm. There is not much influence of the mesh refinement on the results, which supports the use a of one-dimensional model discussed earlier to determine mesh spacing. However, the predictions of small-scale secondary instabilities are strongly influenced by mesh spacing as can be seen in Fig. 13. Note that the secondary instabilities are not symmetric and hence the full computational domain must be used unlike the one shown in Fig. 4. Decreasing the mesh

spacing (Δx) also implies decreasing the time step (Δt) so as to keep the ratio $\Delta x/\Delta t$ constant. Hence when the mesh spacing is halved, the computational time increases by a factor of 8. The computations were performed on a Linux cluster consisting of 128 parallel processors (256 MB RAM per CPU). The computational time for varying mesh spacings is shown in Table 2. Considering all these factors, we decided to keep the final mesh spacing as 50 μm. Henceforth, numerical simulations imply a full computational domain with 50 μm as the mesh spacing.

Table 2
Computational Time.

Mesh Size (μm)	Computational Time
200	1.36 hours
100	10.9 hours
50	3.6 days
25	29 days
12.5	232 days

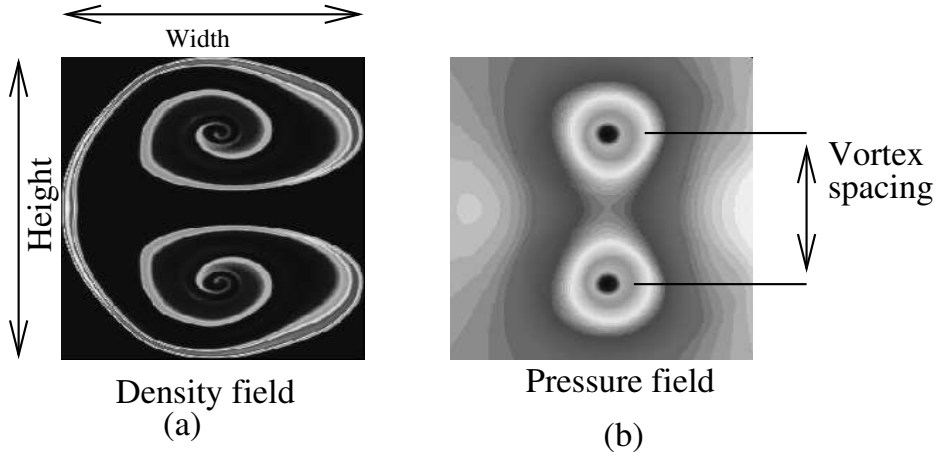

Fig. 9. (a) The width and height of the mixing zone produced by shock-acceleration of the SF_6 cylinder. (b) Vortex spacing. Dark region corresponds to air in density field and low pressure in pressure field.

4.2 Qualitative comparison

The qualitative comparison of flow fields acquired in experiments and by our numerical simulation is shown in Fig. 14. The evolution of the vortex pair, including spikes and bubbles, is evident in our simulations. A notch at the axis of symmetry of the cylinder appears in the simulations at earlier times, as can be seen in the experiments as well. This is likely due to shock wave focusing.

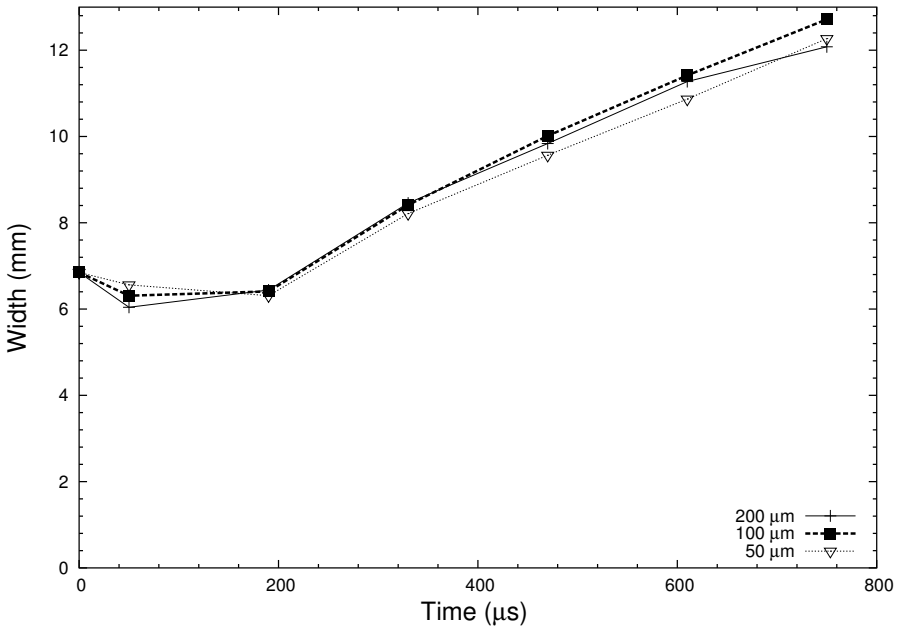

Fig. 10. Effect of mesh spacing on the mixing zone width.

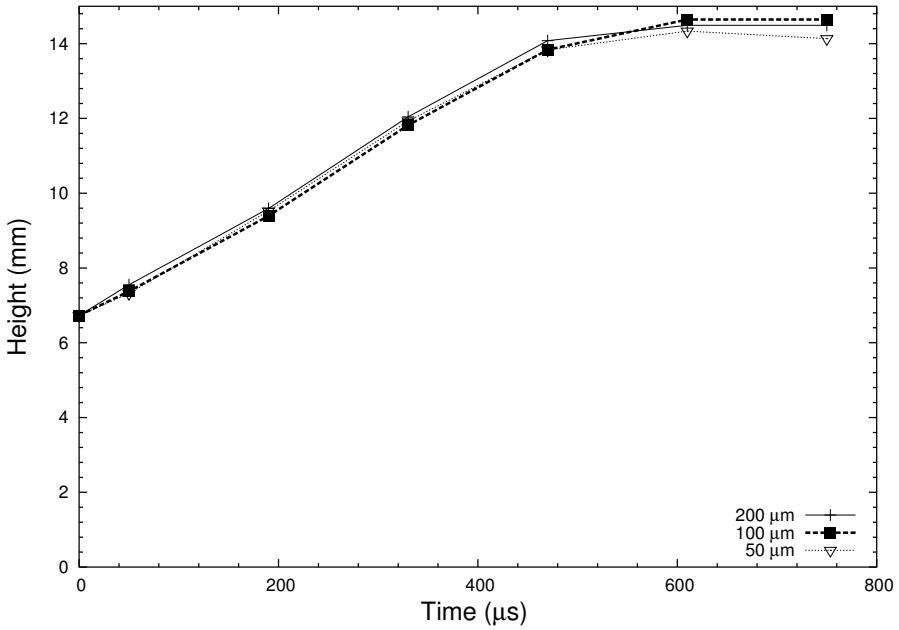

Fig. 11. Effect of mesh spacing on the mixing zone height.

The cylinder appears to evolve somewhat slower in the simulations and also the small-scale structures appear at later times than observed in experiments. This could indicate a problem with vorticity deposition during the initial stage of the RMI simulation. For a future study elucidating the issue, it would be highly desirable to procure early-time experimental velocity fields. Zoldi (2002) had performed 2-dimensional simulations using the RAGE code and observed that the cylinder evolves faster in simulations than in experiments.

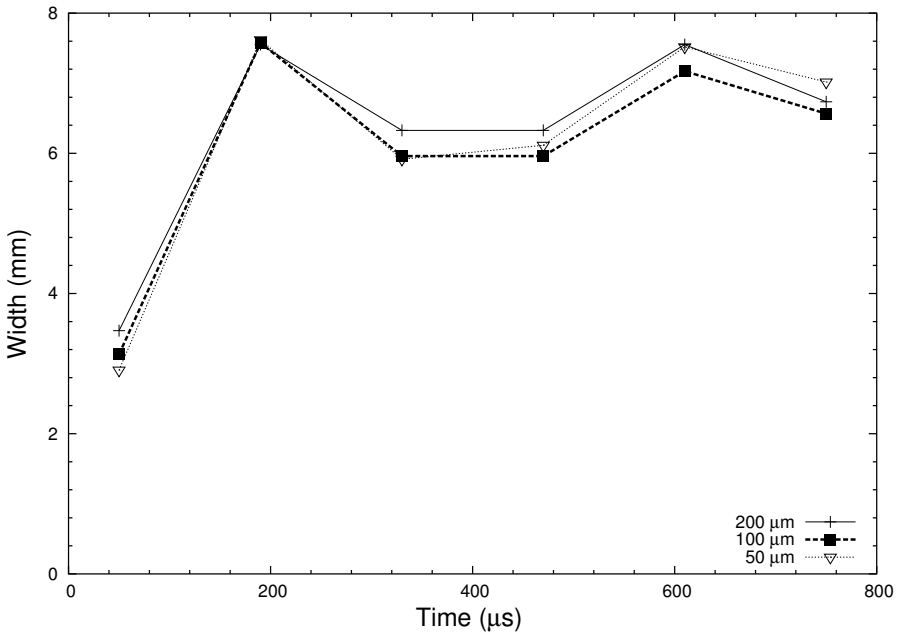

Fig. 12. Effect of mesh spacing on the vortex spacing between two large scale vortices.

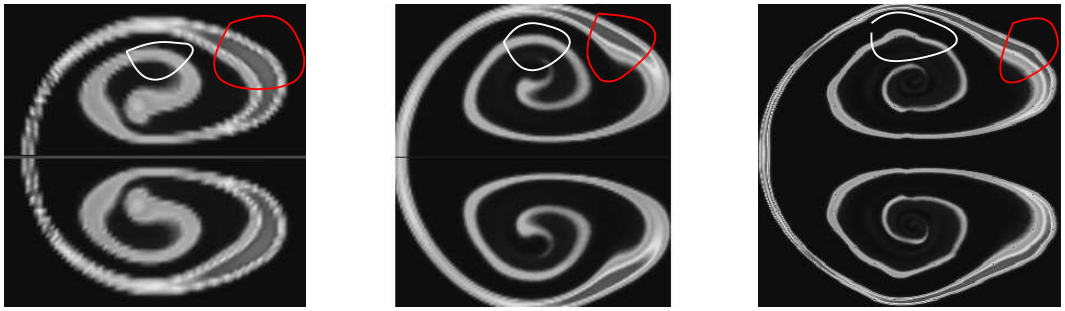

(a) (b) (c)

Fig. 13. Effect of mesh spacing on the development of small-scales. (a) mesh spacing = 200 μm, (b) mesh spacing = 100 μm and (c) mesh spacing = 50 μm

The secondary shear induced instability and baroclinic instability, as explained earlier, are visible in our results. The secondary instabilities in our simulations are compared with these from the simulations of Greenough *et al.* (2001) using the Raptor code at 800 μsec. Fig. 15 shows the comparison for the secondary shear induced instability while Fig. 16 shows the comparison for the secondary baroclinic instability.

4.3 Quantitative comparison

The height and width of the mixing zone (defined as the horizontal and vertical extent of the perturbed SF_6 cylinder), and the vortex spacing are used for

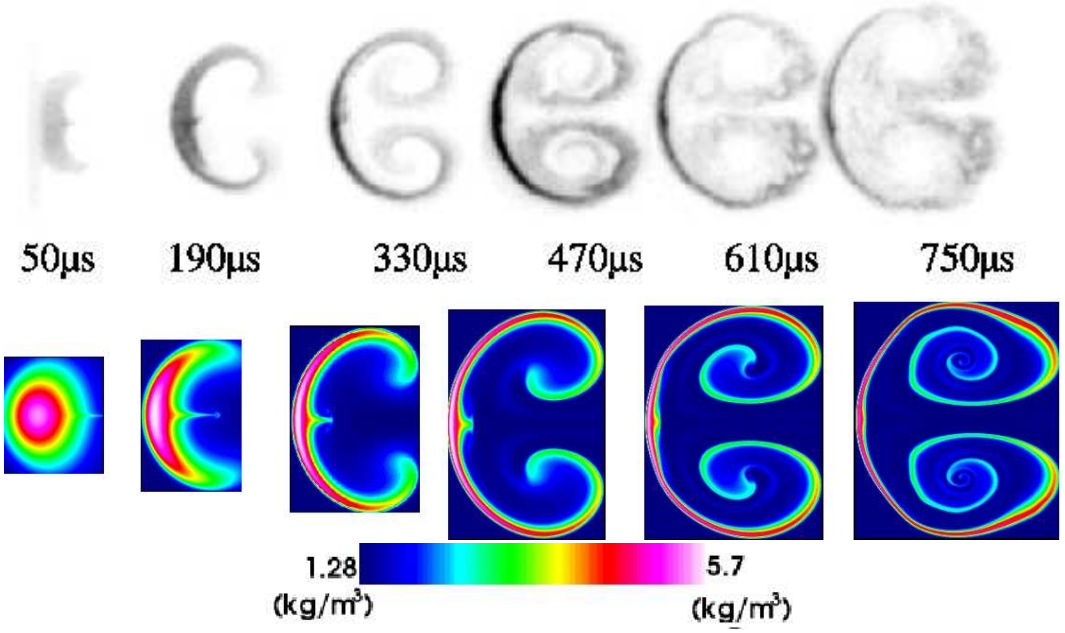

Fig. 14. Comparison of experiment (top) and our numerical simulation (bottom). In experimental images dark color coressponds to higher SF_6 concentration. In numerics blue color corresponds to air.

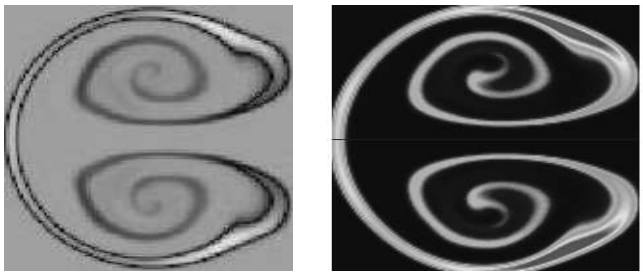

(a) (b)

Fig. 15. Prediction of secondary shear induced instability. (a) : results obtained by Raptor for 125 μm mesh size(Greenough *et al.*, 2001). (b) : our result for 100 μm mesh size.

quantitative comparison between experiment, our simulation and the simulation done by Greenough *et al.* (2001). Vortex spacing from experiments was not available for early times and was not available at all from Greenough *et al.* (2001). These comparisons are shown in Fig. 17, 18 and 19. The results show that the overall trend of our simulation is consistent with the experiments as well as the simulations done by Greenough *et al.* (2001). The differences between our results and the experiments is very close to that between predictions of Greenough *et al.* (2001) and experiments. Zoldi (2002), with RAGE code found similar differences with RAGE code as well. This illustrates the often-overlooked point that quantitative agreement between two simulations does not necessarily mean that the same degree of agreement exists between either of the simulations and the experiment.

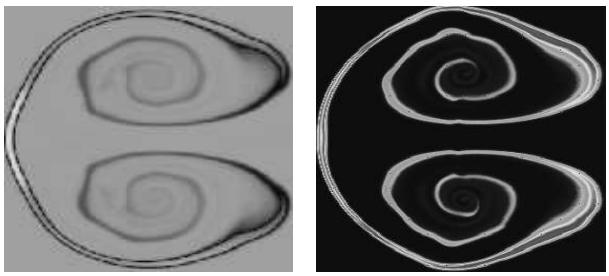

(a) (b)

Fig. 16. Prediction of secondary baroclinic instability. (a) : results obtained by Raptor for 62.5 μm mesh size (Greenough *et al.*, 2001). (b) : our results for 50 μm mesh size.

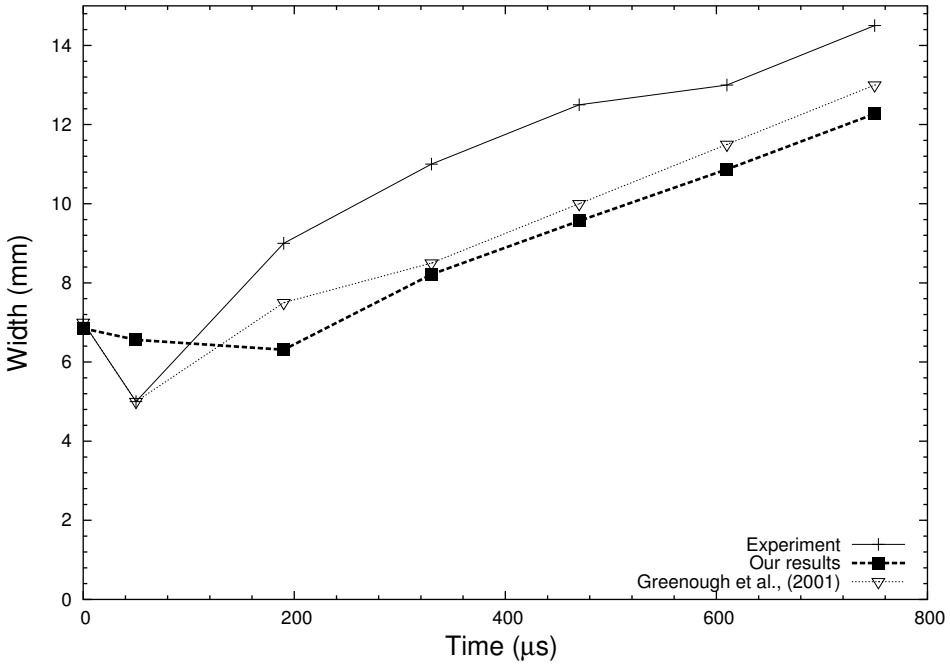

Fig. 17. Mixing zone width: comparison between experiment and numerics.

4.4 Elliptical Initial Conditions

The work described above used circularly symmetric Gaussian density distribution for the initial conditions. However, in experiments the initial conditions are always subjected to small perturbations. To simulate the effect of such perturbations on the evolution of the flow, we introduced small deviations into the initial conditions as follows. The circular distribution was replaced with a slightly elliptical one, with the ratio between the major and the minor axis 1.05. The angle θ between the major axis of the ellipse and the direction of the shock was varied in increments of 22.5° between 0° and 90°, resulting in five sets of the initial conditions.

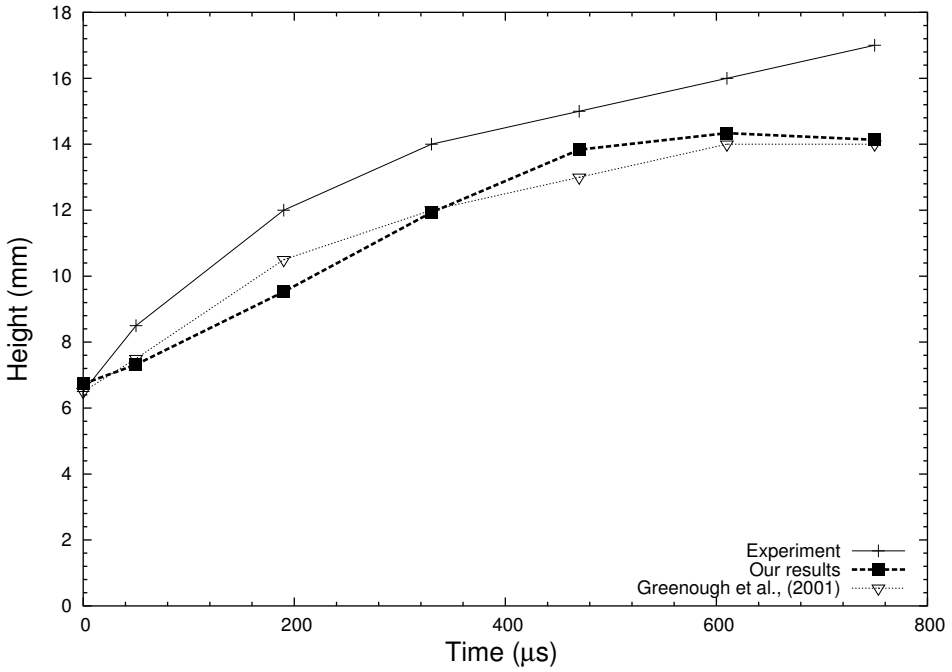

Fig. 18. Mixing zone height: comparison between experiment and numerics.

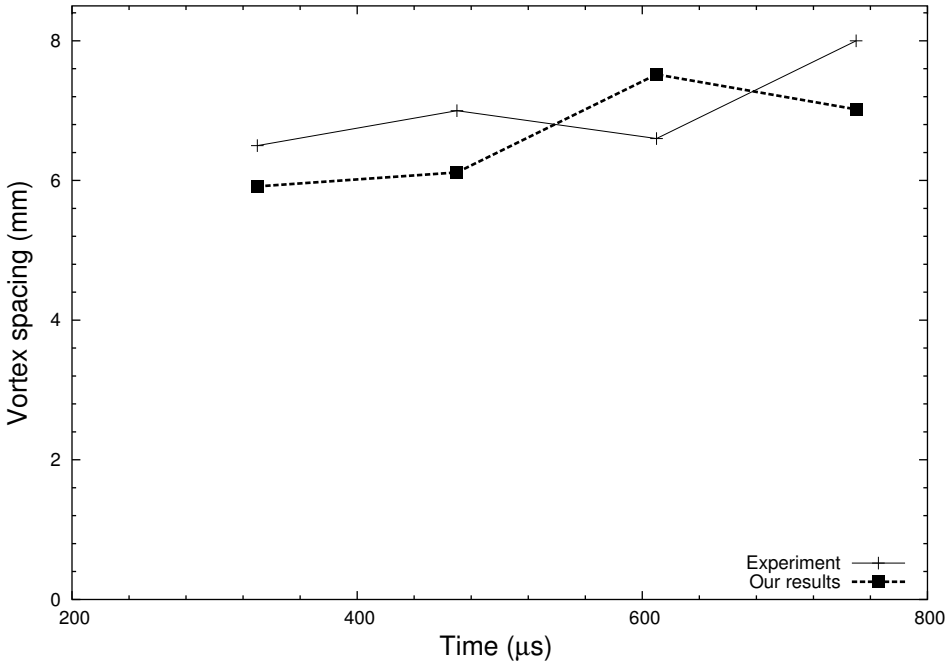

Fig. 19. Comparison for vortex spacing

Figure 20 shows the evolution of the flow developing from these initial conditions in our simulation. At early times, variation of the initial conditions has little influence on the apparent flow structure. The only flow feature directly affected is the spike produced by shock focusing (Fig. 20, top row closeups). Loss of symmetry along the centerline in the direction of the shock propaga-

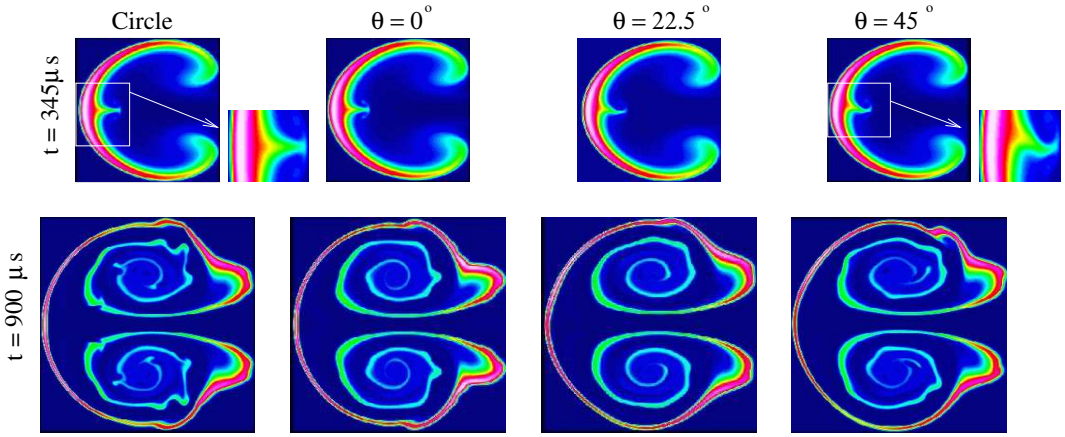

Fig. 20. Flow morphology for different initial conditions. Top : at time = 345 μs and bottom : at time = 900 μs. The first image in both rows corresponds to the circular distributions while all other images are for elliptical conditions. Closeup shows the notch.

tion leads to the distortion of the spike very similar to that observed in most experiments.

At late times, the overall flow morphology remains the same, manifesting the large-scale structure produced by the initial RMI-induced vorticity deposition and the smaller structures emerging due to the secondary instabilities. The specific features of these small-scale structures (e.g., position) vary for different θ, in a fashion similar to that observed in experiment for initial conditions with small perturbations inherently present. Thus it can be concluded that in the "viewgraph norm" the simulation agrees with the experiment. Moreover, the simulation captures an important feature of the RMI-driven cylinder flow in the stage of incipient turbulence: while the large-scale structure is reliably reproducible from experiment to experiment, the small scales are disordered. In the simulation, this disordering is produced by a subtle change in the initial conditions.

In the analysis of experimental measurements, both the density fields (Tomkins *et al.*, 2003) and the velocity fields (Vorobieff *et al.*, 2003)) have been ensemble-averaged. One could expect quantitative agreement between these ensemble-averaged results and similar results from a RANS code. By subtracting the ensemble average from the instantaneous experimental fields, fluctuation fields were produced as well. Statistical analysis of the instantaneous, ensemble-average and fluctuation velocity fields (Vorobieff *et al.* (2003)) acquired in experiment as the flow transitions to turbulence revealed some interesting trends. The statistics of the flow were analyzed in terms of the longitudinal velocity structure functions

$$S_n(r) = \left\langle \left[(\mathbf{u}(\mathbf{x}+\mathbf{r}) - \mathbf{u}(\mathbf{x})) \cdot \frac{\mathbf{r}}{|\mathbf{r}|} \right]^n \right\rangle,$$

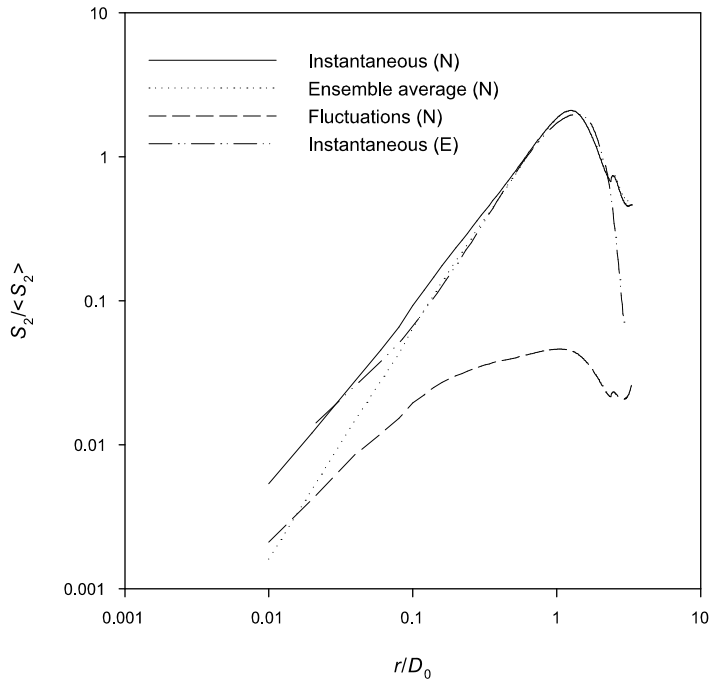

Fig. 21. Second-order longitudinal velocity structure functions of instantaneous, ensemble-averaged and fluctuating velocity fields obtained from elliptic ICs (see text) at ~ 900 μs. The structure functions are normalized by their average value, the scale r is normalized by the nominal gas cylinder diameter D_0. The second-order velocity structure function obtained in experiment (Vorobieff *et al.* (2003)) at ~ 760 μs is shown for comparison. Experimental and numerical data are labeled 'E' and 'N' correspondingly in the captions.

where $r = |\mathbf{r}|$ and $< \cdots >$ denotes ensemble-averaging. For the second-order velocity structure function $S_2(r)$, it was found that the late-time (~ 1300 μs) behavior of the instantaneous field structure function approaches the $2/3$ power law, consistent with Kolmogorov's 1941 theory of fully developed turbulence. This result was not altogether surprising, as the flow is transitioning to turbulence. What was more interesting was the emergence of the similar behavior at a much earlier time (~ 760 μs) in the structure functions of the *fluctuating* velocity. These observations were based on the measurements of two velocity components in a plane normal to the axis of the cylinder, with an effective grid resolution of about 70 μm. The question that arises quite naturally is whether the same trends can be observed in the analysis of our numerical data.

Figure 21 shows the structure functions $S_2(r)$ produced by the analysis of the velocity fields at ~ 900 μs developing from the elliptic initial conditions described above. It is noteworthy that the overall agreement of the instantaneous and ensemble-averaged structure function behavior with experiment is

fairly good. Also like in experiment, the behavior of the fluctuating velocity structure function is distinctly different. Here, however, is where the similarity between experiment and theory ends. While the fluctuating velocity field structure function in experiment shows a trend towards 2/3 power-law scaling starting as early as $\sim$ 760 μs, the fluctuating components of the numerical data exhibit a distinctly different behavior, with the fluctuation structure function S_2 growth with r falling far short of the 2/3 power law. Is this surprising? Perhaps it should not be, as the fluctuating features in experiment are three-dimensional, while the similar features in numerics are confined to two dimensions, and no simple increase in grid resolution is likely to eliminate this problem, even if the 2D grid resolves the Kolmogorov scale. In the latter case, analysis of fluctuations in the flow developing from small changes in the initial conditions is likely to reveal statistics consistent with those predicted and experimentally observed for spatially two-dimensional turbulence (see, for example, Vorobieff *et al.* (1999)). The latter leads to scalings distinctly different from those predicted by the Kolmogorov theory and observed in 3D experiments. Thus the comparison of the fluctuating component scalings in experiment and numerics reveals an important physics issue of limitations inherently present in a 2D simulation of a spatially 3D unstable flow.

4.5 Effect of viscosity and peak SF_6 concentration

In simulations performed for an inviscid case, there was no appreciable difference observed in the results. This supports the notion that viscous dissipation is of relatively small importance on the time scale considered here (< 1000 μs). We also performed the simulations for 60% peak SF_6 concentration. In this case, the SF_6 cylinder seems to evolve at a faster rate and also the secondary instabilities were observed at times much earlier than the 80% case. This can be attributed to steeper gradient in the Gaussian distribution for 60% case (so that the total concentration of SF_6 is the same in both cases) as compared with the 80% case. Steeper gradients in density fields imply stronger baroclinic deposition and hence faster evolution of the SF_6 cylinder. For space constraints, the results are not presented here. The peak concentration of SF_6 in the initial conditions in experiment is subject to some fluctuations, and an accurate measurement of the initial concentration field, as well as the early-time velocity field, as mentioned earlier, should help resolve the discrepancy. Zhang *et al.* (2004) have recently adopted a feed-back kind of approach to resolve the uncertainty in experiments. They have used a finite thickness layer located between SF_6 and air. The parameters of this finite layer are changed with iterations till good agreement is achieved between the simulations and experiments (Peng *et al.*, 2003; Zhang *et al.*, 2004). Zoldi (2002) also concluded such need to change the initial density distribution to achieve better agreement with experiments. However, such approaches cannot be used to validate

CFD codes as they already have the implicit confidence in the CFD code.

5 Conclusion

We have performed a two-dimensional numerical simulation of a popular validation problem involving shock acceleration of an initially diffuse heavy-gas (SF_6) cylinder embedded in lighter gas (air). Unlike many earlier simulations, this work uses a relatively simple code (*e.g.*, no adaptive mesh refinement) and limitied computational resources, nevertheless producing an overall good agreement with experiment.

We use one-dimensional modeling of a moving shock to produce a reasonable estimate of the mesh size. Our results show the evolution of vortex pair, development of spike and bubble, and the notch at the axis of symmetry of the cylinder which are consistent with the experiments. Both secondary instabilities, shear induced and baroclinic, are predicted by our simulations and are consistent with the numerical predictions of Greenough *et al.* (2001). The quantitative comparisons show that our results have the same overall trend as observed in experiments and other simulations. Our qualitative comparison reveals that the SF_6 cylinder evolves slower in the simulations, particularly at early times, and also that the evolution of the developing small scales differs from the experimental observations. Viscous effects are shown to be negligible in our RMI simulations while the peak SF_6 concentration does influence the baroclinic deposition and hence also the subsequent evolution of SF_6 cylinder.

Fluctuations in the initial SF_6 distribution have negligible effects on the large scale structure of RMI-driven flow. Loss of symmetry along the centerline in the direction of shock propagation leads to the asymmetry in the notch observed at early times. The second order longitudinal velocity structure functions have revealed the limitations of 2D simulations in predicting the scalings of incipient turbulence which is distinctly different from that predicted by the Kolmogorov theory and observed in 3D experiments. This also suggests that prediction of small scales in RMI by 2D CFD codes does not provide more insight in validation with 3D experiments and in this case code to code comparison may be more useful.

Our code validation exercise has developed confidence in GASP. Hence, like FLASH (Peng *et al.*, 2003; Zhang *et al.*, 2004), RAGE (Zoldi, 2002) and Raptor (Greenough *et al.*, 2001), now GASP can also be used to get more insight in shock-accelerated flows and contribute towards understanding of the complicated hydrodynamics of such flows.

Acknowledgements.

This research was partially supported by Los Alamos National Laboratory, Task Order BG-109 and by the Missile Defense Agency through the Air Force Research Laboratory/Phillips Site and Boeing LTS. Our thanks to Tim Madden, Bill Rider, Jim Kamm, and Cindy Zoldi.

References

Aerosoft, Company Background and History. Cited 24 March 2004. http://www.aerosft.com/Misc/aboutus.php

Arnett, W., Bahcall, J., Kirshner, R., and Woosley, S., 1989. Supernova 1987A. Annu. Rev. Astron. Astrophys., **27**, 629-700.

Budzinski, J. M. and Benjamin R. F., July 1994. Influence of initial conditions on the flow patterns of a shock-accelerated thin fluid layer. Phys. Fluids, **6 (11)**, 3510–3512.

Fishbine, J. M., 2002. Code validation experiments - a key to predictive Science. Los Alamos Research Quarterly.

Greenough, J. A ., Rider, W. J., Zoldi, C., and Kamm, J. R., November 2001. Code-to-code comparisons for the problem of shock acceleration of a diffuse dense gaseous cylinder. 54th annual meeting of the Divisions of Fluid Dynamics, San Diego, CA.

Lindl, J. D., and Mead, W. C., 1975. Two dimensional simulation of fluid instability in laser fusion pellets. Phys. Rev. Lett., **34**, 1273.

Marble, F. E., Hendricks, G. J, and Zukoski, E. E, 1987. Progress towards shock enhancement of supersonic combustion process. AIAA paper, 87-1880

Meshkov, E. E, 1969. Instability of the interface of two gases accelerated by a shock wave. Sov. Fluid Dyn., **4(5)**, 151–157.

Peng, G., Zabusky, N. J., and Zhang, S., 2003. Vortex-accelerated secondary baroclinic vorticity deposition and late-intermediate time dynamics of a two-dimensional Richtmyer–Meshkov interface. Phys. Fluids, **15(12)**, 3730–3744.

Richtmyer, R. D., 1960. Taylor instability in shock-acceleration of compressible fluids. Commun. On Pure and Appl. Math., **13**, 297–319.

Rightley, P. M., Vorobieff, P. and Benjamin, R. F., 1997. Evolution of a shock-accelerated thin fluid layer. Phys. Fluids, **9(6)**, 1770–1782.

Rightley, P. M., Vorobieff, P., Martin, R., Benjamin and R. F., 1999. Experimental observations of the mixing transition in a shock-accelerated gas curtain. Phys. Fluids, **11(1)**, 186–200.

Tomkins, C., Prestridge, K., Rightley, P., Vorobieff, P. and Benjamin, R., 2002. Flow morphologies of two shock-accelerated gas cylinders. Journal of Visualization, **5 (3)**, 273–283.

Tomkins, C., Prestridge, K., Rightly, P., Marr-Lyon, M., Vorobieff, P. and Benjamin R., April 2003. A quantitative study of the interaction of two Richtmyer-Meshkov-unstable gas cylinders. Phys. Fluids, **15 (4)**, 986–1004.

Velikovich, A. L. and Dimonte, G., 1996. Nonlinear perturbation theory of the incompressible Richtmyer-Meshkov instability. Phys. Rev. Lett., **76(17)**, 3112–3115.

Vorobieff, P., Rivera, M.K., and Ecke, R.E., 1999. Soap film flows: Statistics of two-dimensional turbulence. Phys. Fluids, **11(8)**, 2167–2177.

Vorobieff, P., Mohamed, N. G., Tomkins, C., Goodenough, C., Marr-Lyon, M. and Benjamin, R. F., December 2003. Scaling evolution in shock-induced transition to turbulence. Physical Review E, **68**, 065301–065304

Vorobieff, P., Tomkins, C., Kumar, S., Goodenough, C., Mohamed, N.G. and Benjamin, R.F., 2004. Secondary instabilities in shock-induced transition to turbulence. Advances in Fluid Mechanics V, eds. Brebbia, Mendes and Rahman, WIT press, Southampton, UK/Boston, USA, 139.

Yang, Y., Zhang, Q. and Sharp, D. H., 1994. Small amplitude theory of Richtmyer-Meshkov instability. Phys. Fluids, **6(5)**, 1856–1872.

Zhang, Q. and Sohn, SI., 1996. An analytical nonlinear theory of Richtmyer-Meshkov instability. Phys. Lett. A, **212(3)**, 149–155.

Zhang, S., Zabusky, N. J., Peng, G., and Gupta, S., 2004. Shock gaseous cylinder interactions: Dynamically validated initial conditions provide excellent agreement between experiments and numerical simulations to late-intermediate time. Phys. Fluids, **16(5)**, 1203–1216.

Zoldi, C. A., 2002. A numerical and experimental study of a shock-accelerated heavy gas cylinder. PhD. Dissertation, Dept. of Applied Mathematics and Statistics, State University of New York, Stony Brook, NY.